

<https://doi.org/10.1038/s43247-023-00985-1>

OPEN

Cyclones modulate the control of the North Atlantic Oscillation on transports into the Barents Sea

Finn Ole Heukamp ¹✉, Lars Aue ², Qiang Wang ¹, Monica Ionita ^{1,3}, Torsten Kanzow^{1,4},
Claudia Wekerle ¹ & Annette Rinke ²

The warm Atlantic Water transported into the Barents Sea plays a crucial role in winter sea ice extent, marine ecosystems, and mid-latitude weather. The North Atlantic Oscillation is known to be an important driver for the Atlantic Water transport variability in the Barents Sea Opening. Here, we find that the dependence of the Barents Sea Opening ocean volume transport variability on the North Atlantic Oscillation is non-stationary. Our results indicate that for the period 1995 to 2005, the link between the North Atlantic Oscillation and the transport variability in the Barents Sea Opening temporarily weakened before an eventual recovery. During this period, synoptic cyclones with unusual trajectories as a consequence of pronounced atmospheric blocking in the North Atlantic sector altered the large-scale and local wind patterns. This temporarily caused a state that the Barents Sea Opening transport variability is largely locally driven instead of being driven by the North Atlantic Oscillation. Our study suggests that an adequate representation of both the North Atlantic Oscillation and cyclone activity is necessary for climate models to better predict future changes in poleward ocean heat transport and Arctic climate.

¹ Alfred-Wegener-Institute, Helmholtz Center for Polar and Marine Research, Bremerhaven, Germany. ² Alfred-Wegener-Institute, Helmholtz Center for Polar and Marine Research, Potsdam, Germany. ³ Faculty of Forestry, Stefan cel Mare University of Suceava, Suceava, Romania. ⁴ Faculty of Physics/Electrical Engineering, University of Bremen, Bremen, Germany. ✉email: finn.heukamp@awi.de

The Barents Sea (BS) is one of the two major oceanic gateways for warm and saline Atlantic Water (AW) to enter the Arctic Ocean. The temperature and volume, thus oceanic heat, of the AW entering the BS fundamentally shape winter sea ice conditions and air–sea fluxes in the BS^{1,2}. The extent of the sea ice and the strength of air–sea heat exchange are crucial for marine ecosystems and local fishery^{3,4}, European winter weather^{5,6} and terrestrial climate⁷, as well as shipping routes⁸.

The warm AW originates from the tropical Atlantic Ocean. As part of the Atlantic Meridional Overturning Circulation, it is transported north by the Gulf Stream and the North Atlantic Current before reaching the Nordic Seas and finally the Arctic basin⁹. On its way north, most of the AW entering the BS is carried by the Norwegian Atlantic Slope Current (NASC)^{10–13}. From its entry point into the Norwegian Sea to Fram Strait, the NASC exhibits a quasi-simultaneous flow variability, implying that the volume transport variations are driven by the large-scale wind fields over the Nordic Seas domain¹⁴. In addition, the wind stress curl over the North Atlantic affects the interannual variability of the NASC volume transport from upstream¹⁵.

The AW enters the BS as a multi-core current through the central Barents Sea Opening (BSO). The northern part of the BSO is dominated by cold and relatively fresh Polar Water on the Svalbard shelf and a strong and confined westward-directed current south of Bear Island at $\sim 74.3^\circ\text{N}$, transporting Polar Water and modified AW out of the BS¹⁶. Along the Norwegian coast, the Norwegian Coastal Current carries low-salinity water into the BS. The observational estimate of the net BSO volume transport is 2.3 Sv¹⁷. Concerning the individual components, the Norwegian Coastal Current inflow is estimated to be 1.2 Sv, the central BSO inflow is about 2 Sv, and the westward-directed current at the Bear Island slope roughly balances the Norwegian Coastal Current volume transport, transporting about 1.2 Sv out of the BS^{17,18}. The magnitude of the outflow is linked to the wind stress curl over the Svalbard shelf and the flow direction, on daily timescales, can reverse in the presence of strong cyclonic wind anomalies^{16,19}. The main AW pathways toward the Arctic and the main currents in the BSO are shown in Fig. 1. Although long-term in situ ocean current measurements are sparse in the BSO, observations and model studies agree that strong variability in the ocean volume transport through the BSO is linked to both local^{18–22} and remote^{20,22,23} wind forcing. For the latter, the North Atlantic Oscillation (NAO), as a leading mode of sea level pressure (SLP) variability over the North Atlantic, is suggested to play a dominant role^{15,20}.

The NAO pattern can be characterized as an air pressure dipole of the Icelandic Low and the Azores High. It is usually computed as the first empirical orthogonal function of the SLP in the North Atlantic sector, and the associated principal component time-series is taken as the NAO index^{24–26}. The NAO is associated with a certain wind anomaly pattern, whose sign and strength influence ocean heat content and gyre circulation in the North Atlantic and Nordic Seas²⁶. Increased northward winds along the Norwegian coast associated with a positive NAO cause a narrowing and strengthening of the NASC and enhanced BSO inflow^{21,27}. Thus, a narrower and strengthened NASC results in (i) less surface heat loss in the Norwegian Sea and consequently warmer AW temperature, and (ii) increased volume transport through the BSO because the NASC resides closer to the coast so that a larger portion of AW enters the BS²².

After being predominantly negative in the 1970s and 1980s, the winter NAO shifted to a positive state in the early 1990s²⁴ with a related increase in AW transport toward the Arctic Ocean²⁸. From the mid-1990s onward, the NAO index has been neither predominantly positive nor negative but strongly fluctuates from

year to year. There was a high correlation between NAO and BSO AW volume transport as well as BS sea ice cover before 2000, but the correlation broke down around the year 2000¹⁸. The cause for the breakdown is yet unknown and represents a major focus of this study.

In addition to the large-scale forcing, local SLP anomalies, e.g., associated with synoptic cyclones, can also have a significant impact on the transport through the BSO^{16,19}. In general, the frequency and the path of cyclones in high latitudes are influenced by large-scale atmospheric conditions. Particularly the NAO has a strong influence on the winter storm tracks, with a positive (negative) NAO phase tending to increase (decrease) the frequency of cyclones in the vicinity of the climatological mean position of the Icelandic Low as well as in the Norwegian Sea^{29,30}. In addition, the occurrence of atmospheric blocking and local baroclinicity, mainly influenced by upper-level winds and the jet stream, are important drivers of the variability of cyclone tracks in higher latitudes²⁹.

In this study, we disentangle the local and upstream forced contributions to transport anomalies through the BSO and evaluate their individual dependence on the NAO. We show that transport anomalies forced upstream at the Norwegian Atlantic coast are strongly bound to the NAO. This dependence, however, is not constant but varies in time. We further attribute a pronounced temporary breakdown of the co-variability between the BSO transport anomalies and the NAO in the 1995–2005 period to the anomalous occurrence of synoptic cyclones, affecting key regions relevant to the forcing of the BSO transport.

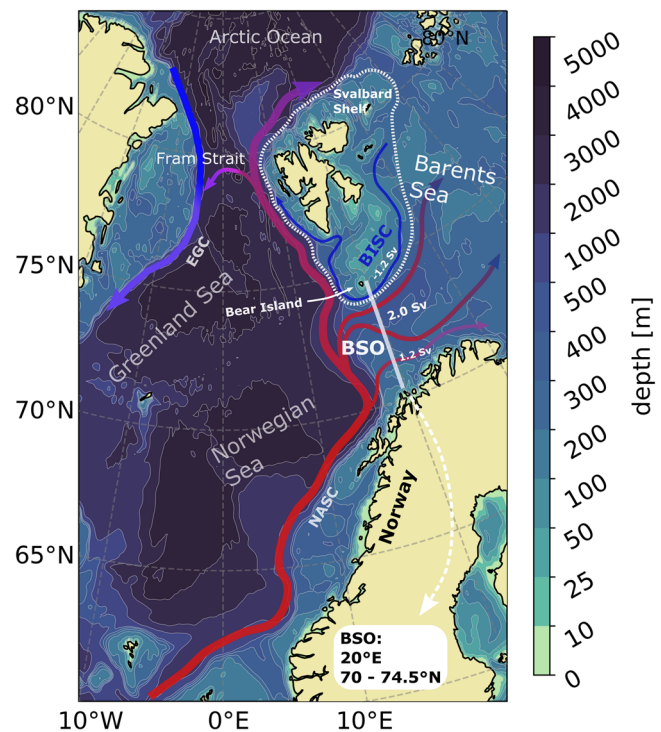


Fig. 1 Atlantic Water pathway through the Nordic Seas into the Barents Sea and Arctic Ocean. Overview of bathymetry, main currents transporting Atlantic Water towards the Arctic Ocean, and names of important islands, seas and currents. The BSO section where transports are evaluated in the model is highlighted by a white line. The wider shelf of Svalbard is encircled by a dashed white line. EGC East Greenland Current, NASC Norwegian Atlantic Slope Current, BSO Barents Sea Opening, BISC Bear Island Slope Current.

Results

(Co-)variability of local/upstream forced Barents Sea Opening transport and the North Atlantic Oscillation. The NAO, as the leading climate pattern in the North Atlantic sector, has a major impact on the transports through the BSO. Composite maps of 850 hPa geopotential height anomalies during winters with extraordinarily strong/weak net transports through the BSO (in CTRL, see “Methods”) reveal a spatial structure that well resembles the air pressure dipole and wind anomalies associated with the NAO (Fig. 2 and Supplementary Fig. S1). For assessing the impact of the NAO on different components of the transport variability in the BSO, however, a separation of the transport components is needed. In order to separate the upstream and locally forced contributions to the interannual variability of the transport through the BSO, we carried out three dedicated model simulations with the global sea ice and ocean model FESOM2.1³¹: one control simulation, with the same reanalysis forcing everywhere (CTRL), one where a normal year forcing (similar to atmosphere climatology, see “Methods”) replaces the reanalysis forcing in the Arctic (ArcClim), and one where the reanalysis

forcing outside the Arctic is replaced with the normal year forcing (ArcVari, see “Methods” for details).

By combining reanalysis and normal year forcing in ArcVari and ArcClim we are able to split the total transport anomalies in CTRL into their upstream (outside Arctic domain) and locally (inside Arctic domain) forced components. We found that the results of the ArcVari and ArcClim simulations are linearly additive to reproduce the CTRL variability²² (Fig. 3a). The standard deviations of the winter BSO net transport anomalies (1970–2019) are 0.35 Sv in ArcVari, 0.31 Sv in ArcClim, and 0.58 Sv in CTRL. The comparable magnitudes of the variations indicate a similar contribution from the locally and upstream forced variability to the total transport variability in the BSO (Fig. 3a). In addition, we split the net transport anomalies into those arising from inflowing water (eastward flow) and from outflowing (westward flow) water (Fig. 3c, e). The BSO inflow variability (standard deviation of the eastward transport) is 0.55 Sv in CTRL, which evenly splits into one part forced locally (ArcVari: 0.24 Sv), and another part forced upstream (ArcClim: 0.28 Sv). Hence, the inflow is to a similar degree controlled by local and upstream forcing. In contrast, the outflow variability (standard deviation of the westward transport) is reduced by about half when the Arctic atmospheric variability is removed (ArcClim: 0.12 Sv, CTRL: 0.26 Sv). However, when there is only variability in the Arctic atmospheric forcing, the outflow standard deviation is the same as in the control run (ArcVari: 0.26 Sv). This implies the outflow is mainly locally driven.

The separation into local and upstream forced transport anomalies further reveals strong year-to-year variability as well as decadal variations in both ArcVari and ArcClim. The variations of the net transport and inflow are well aligned with the NAO index (Fig. 3a, c), confirming the results of the composite analysis (Fig. 2). For the full 1970–2019 period, the Pearson correlation between the detrended net (inflow, outflow) BSO transport and the detrended NAO index is 0.73 (0.70, 0.39) in CTRL, 0.51 (0.50, 0.23) in ArcVari, and 0.79 (0.71, 0.53) in ArcClim. All standard deviations, correlations, and statistical significance are summarized in the Supplementary Table S1. Our simulations reveal an overall high dependence of net transport variability in CTRL and ArcClim on the NAO state, and the high dependence is mainly attributed to the inflow variability. In contrast, neither locally forced (ArcVari) inflow variability nor outflow variability is as strongly linked to the NAO (Fig. 3a, c, e). Nevertheless, the simulations suggest that during the pronounced negative NAO from the mid-1970s to the end of the 1980s, locally forced transport anomalies (net and inflow) are well aligned with the NAO index (Fig. 3a, c). The correlation seemingly decreases with the shift towards positive NAO in the 1990s. The co-variability of the NAO and the locally and upstream forced transport anomalies thus seems to be subject to decadal variations.

In order to investigate potential decadal changes in the co-variability of different transport components and the NAO, we proceed with computing the Pearson correlation within a moving 11-year window of the timeseries, to capture decadal (co-) variability (Fig. 3b, d, f). The results demonstrate that the co-variabilities of the NAO and CTRL/ArcVari/ArcClim transports are not constant in time (Fig. 3b, d, f). For the net transport, the moving correlations between NAO/CTRL and NAO/ArcClim depict a pronounced minimum during the 1995–2005 period (Fig. 3b). Moreover, locally forced net transport anomalies strongly co-vary with the NAO in the mid-1970s to late 1980s before losing the co-variability at the beginning of the 1990s (Fig. 3b). Similar dependencies are found when considering the inflow (Fig. 3d). The minimum correlation in the 1995–2005 period is even more pronounced and suggests that the NAO loses control especially on the upstream forced inflow in these years.

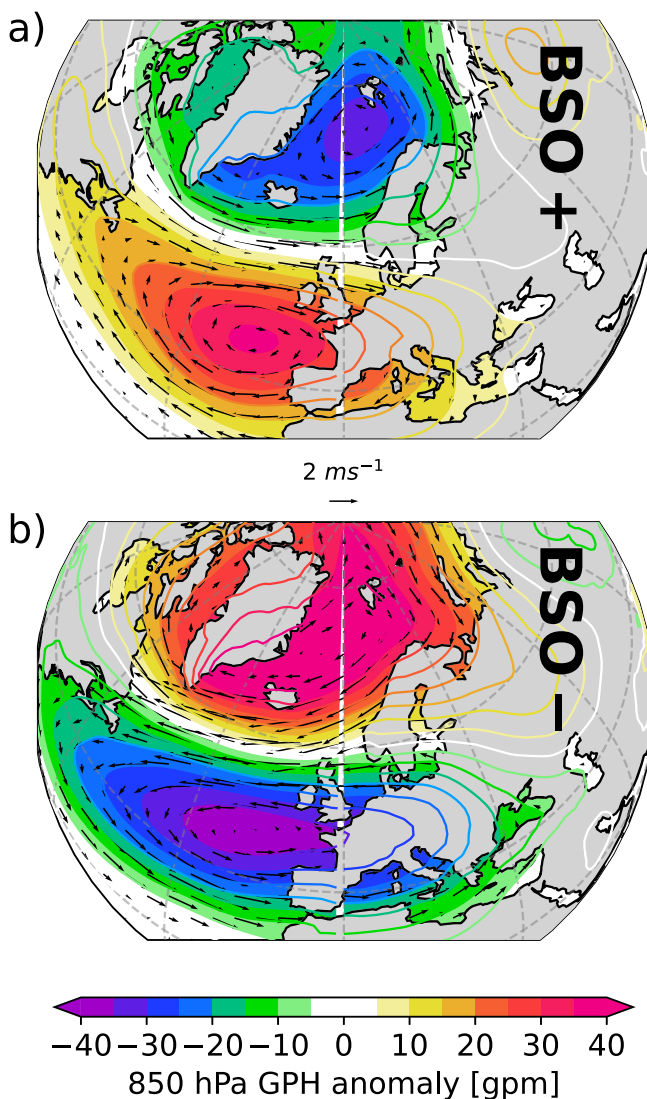


Fig. 2 Large-scale wind and pressure pattern associated with strong and weak Barents Sea Opening transport. Composite maps of 850 hPa geopotential height anomalies and associated wind anomalies (DJFM) during strong (a) and weak (b) net transport through BSO based on JRA55.

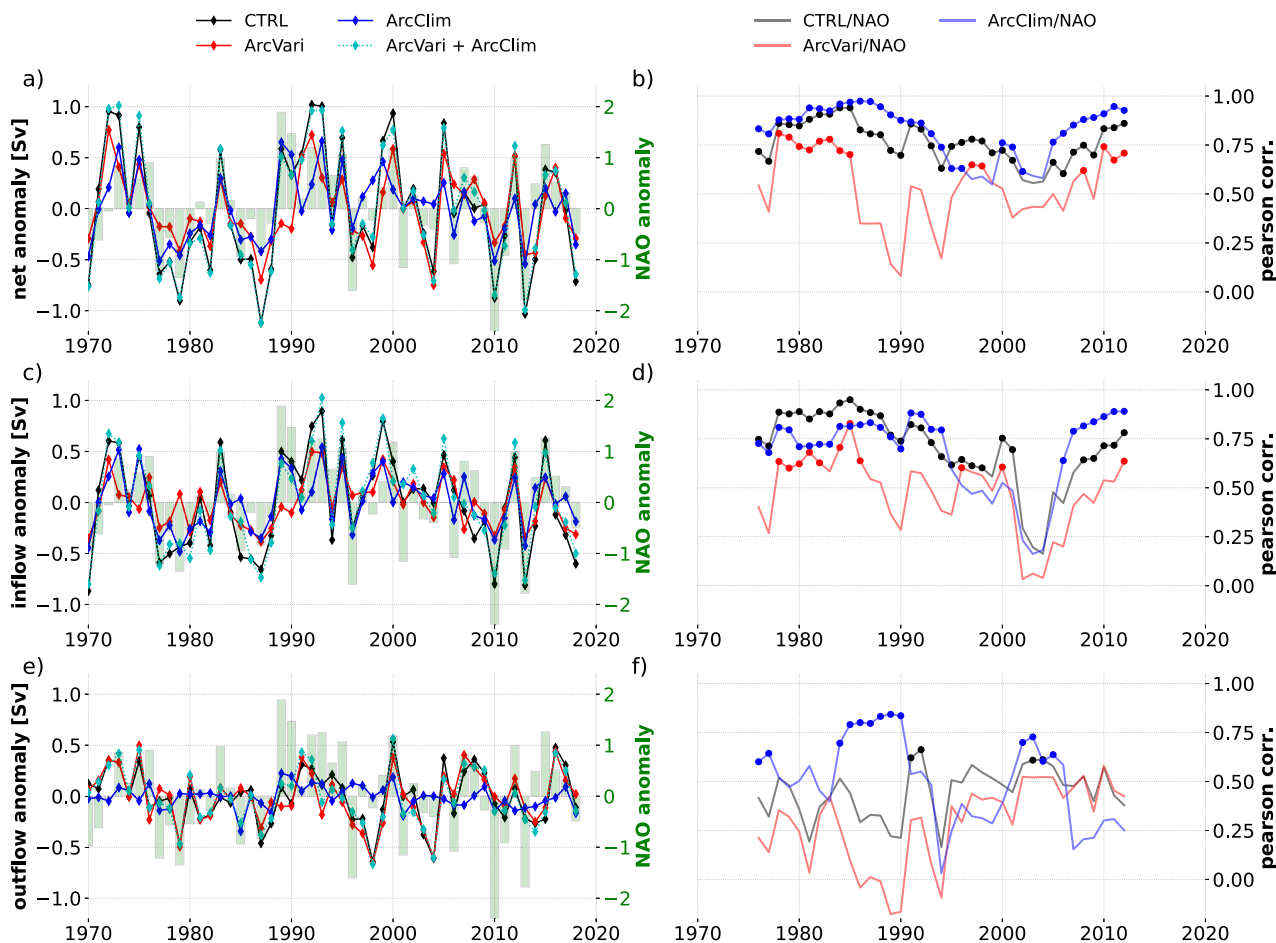


Fig. 3 Changing impact of the North Atlantic Oscillation on transports through the Barents Sea Opening. Net BSO transport anomalies in CTRL, ArcVari (non-Arctic variability removed), ArcClim (Arctic variability removed), and NAO index (a). Moving correlation (11-year window) between CTRL/NAO, ArcVari/NAO, ArcClim/NAO (b). Markers in (b, d, f) highlight statistically significant correlations. Years depict the center of the respective 11-year period. (c–f) Same as in (a, b) but for BSO inflow (eastward transport only) and outflow (westward transport only). In all timeseries presented in (a, c, e), the mean and the linear trend were removed. Note that negative outflow anomalies denote increased (westward) outflow.

In general, inflow variability is comparably weak in the 1995–2005 period. The variability strength (standard deviation) of the inflow reduces to 0.29 Sv in CTRL (–50%, compared to the 1970–2019 period), 0.16 Sv in ArcVari (–34%), and 0.20 Sv in ArcClim (–29%) when only considering the 1995–2005 period. In this period, extraordinary anomalies in the outflow (exceeding 2 standard deviations) occur in two winters (1998: –0.65 Sv, 2004: –0.60 Sv) (Fig. 3e). As already presented, outflow anomalies are forced locally and do not exhibit any statistically significant link to the NAO (95% confidence level). Reduced co-variability between the net BSO transports and the NAO in this time period might thus arise from a combination of a general decrease in the NAO’s ability to control the upstream forced inflow and a simultaneous dominance of the non-NAO related outflow. The interim loss of the NAOs’ ability to control the upstream forced inflow variability suggests a change in the large-scale wind forcing. The concurrent phenomena of the extraordinary outflow anomalies and the breakdown of the NAO control on the upstream forced inflow between 1995 and 2005 could share a common forcing mechanism, which will be explored below.

Interim change of large-scale and local wind patterns controlling the Barents Sea Opening transport variability. Despite that the composite analysis revealed a dominant control of the

NAO on the BSO volume transport (Fig. 2), the analysis of co-variability rather indicates that such a control does not function all the time (Fig. 3). To more precisely identify spatial patterns in the large-scale winds associated with the BSO transport variability and to monitor their robustness in space and time we further perform multivariate regression analysis with the zonal and meridional wind fields used to force the model as predictors of the net transport anomalies (“Methods”). The obtained regression coefficients are used to reconstruct the transport anomalies based on the local wind at every grid cell. Correlating the initial and reconstructed transport anomalies for each grid cell highlights areas most likely to impact the BSO transport. The coefficients of the regression fit at each grid point can further be interpreted as the local preferred wind direction to create anomalies in the BSO transport (“Methods”). As our simulations revealed strong decadal changes in the transport components and especially in their co-variability with the NAO (Fig. 3), we conducted the regressions for the periods 1970–1995, 1995–2005, and 2005–2018 separately.

From 1970 to 1995, the region most important for controlling the BSO net transport anomalies in CTRL is the Norwegian Sea coastal area, where correlations exceed 0.8 (Fig. 4a). The preferred wind direction in this area is along-coast, yielding onshore Ekman transport, an increased sea surface height (SSH) gradient perpendicular to the coast, and thus an acceleration of the NASC, finally leading to increased BSO inflow downstream. The area of most pronounced correlation at the Norwegian coast extends far

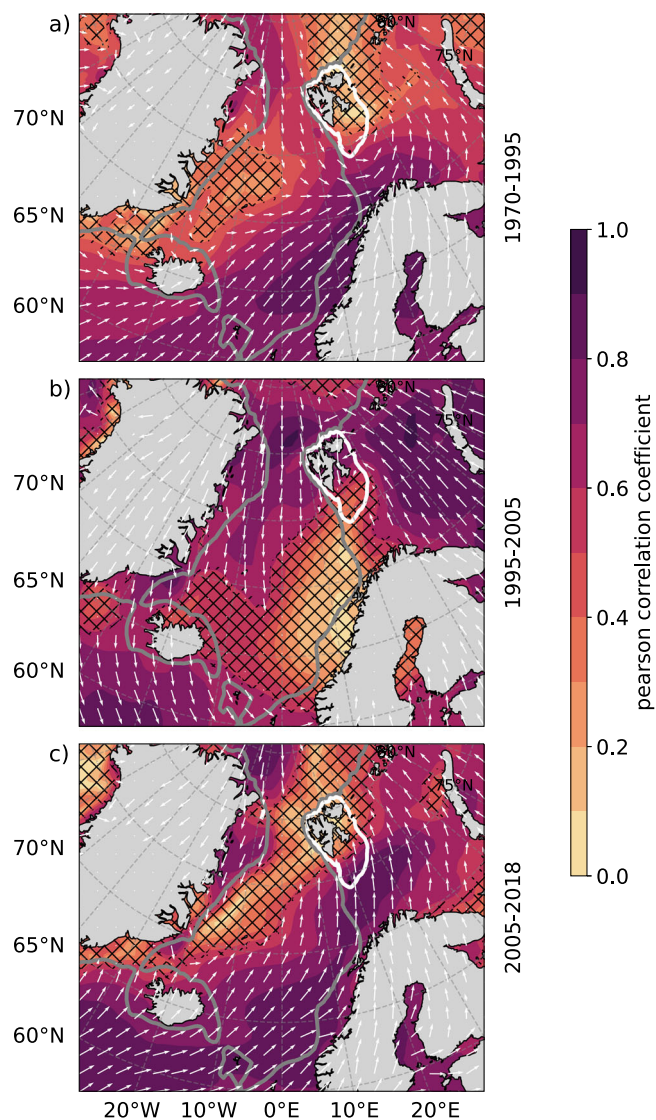


Fig. 4 Areas and wind patterns that can explain transport variability in the Barents Sea Opening. Correlation maps of modeled and reconstructed BSO net transport anomalies in CTRL. The analysis is performed for (a) 1970–1995, (b) 1995–2005, and (c) 2005–2018 separately. Arrows denote preferred wind direction and are scaled by the underlying correlation field. The gray (white) line depicts the 500 m (180 m) isobath. Non-significant correlations are covered by black hatching.

north into the BSO, where the same dynamical mechanism (alongshore winds producing an increased SSH gradient which sets up increased geostrophic flow) locally enhances transport in this period (Fig. 4a). In addition to local and remote alongshore winds perturbing the geostrophic inflow, our regression analysis identifies cyclonic winds centered over the Svalbard shelf as a third driver of BSO net transport variability on interannual timescales (Fig. 4a). Cyclonic wind anomalies over the northern BS shelf/southern Svalbard Bank cause divergent Ekman transport and thus a local reduction in SSH^{16,19}. The negative SSH anomaly weakens the SSH gradient south of Bear Island, thus reducing the outflow and resulting in a positive net transport anomaly. Hence, while alongshore winds control the (both local and upstream forced portion) inflow variability, winds over the Svalbard shelf steer the variability of the outflow. Similar spatial patterns are found in the 2005–2018 period (Fig. 4c). Except for non-significant correlations west of Svalbard, the same forcing

mechanisms as in the 1970–1995 period are dominant. In both periods, the general wind pattern closely resembles the wind pattern associated with the NAO (Supplementary Fig. S1), namely westerly winds south of Iceland that turn southwesterly at the Norwegian coast, and northerly and northeasterly winds along the east Greenland coast.

During the 1995–2005 period when transports through the BSO and the NAO seemingly lose their strong correlation, the spatial pattern of the regression/correlation analysis reveals remarkable differences to the previous and subsequent periods and does not resemble the NAO pattern (Fig. 4b). Instead of the highly correlated areas along the Norwegian coastline, southerly winds in the BS turning westward north of Svalbard and northerly winds in Fram Strait form a cyclonic pattern and seem to be more important for shaping the net transport anomalies in the BSO. This is consistent with the dominance of the outflow variability in this period (Fig. 3a, e).

The wind variability in the Nordic Seas and BS in winter is heavily influenced by synoptic-scale atmosphere variability, especially synoptic cyclones affecting the SLP and wind field^{32,33}. While propagating along the North Atlantic storm track into the Arctic region, cyclones affect the intensity of the alongshore winds driving the NASC. As already pointed out, the westward-directed Bear Island Slope current is also sensitive to cyclones passing over the northern BS shelf¹⁶. In order to understand the observed changes in the large-scale flow affecting the transports through the BSO, we thus further turn our attention to the propagation of cyclones towards the BS.

Anomalous atmospheric blocking and deflection of cyclones weakening the NAO control on BSO transport in the 1995–2005 period. Based on the timeseries presented in Fig. 3c, e, we have identified six anomalous years in this period, when the NAO state and the transport anomalies mismatch: two in terms of extraordinarily strong outflow (1998, 2004; exceeding 2 standard deviations of the locally forced (ArcVari) outflow) and four non-NAO driven inflow anomalies (1994, 2000, 2001, 2005; when the NAO does not relate to the upstream forced transport anomaly (ArcClim), i.e., when the NAO index has the opposite sign to the inflow anomaly) which seemingly contributed to the breakdown of the NAO influence on the transport through the BSO observed in the 1995–2005 period.

In the winters of 1998 and 2004, the net transport anomaly in the BSO is dominated by the extraordinarily strong outflow, which does not reveal any dependence on the NAO (Fig. 3a, e), but is known to be sensitive to local cyclone activity^{16,19}. Considering the anomaly of the SLP and the anomalous surface winds in the winters 1998 and 2004 based on JRA55-do, it becomes evident that both winters are dominated by positive SLP anomalies associated with anomalous anticyclonic winds in the northern BS (Fig. 5a, b). Farther south, close to the Norwegian coast, a negative SLP anomaly associated with anomalous cyclonic winds is found. The wind anomaly patterns are thus similar to those obtained from the regression/correlation analysis for the 1995–2005 period (Fig. 4b), indicating that pronounced local wind anomalies are found in the BS and winds at the Norwegian coast are deflected (not relevant for the inflow anymore). In order to reveal the contribution of synoptic cyclones to the SLP and wind anomalies, and ultimately to the ocean transports, we further conduct analysis of trajectories of cyclones that reach the surrounding of the BS in the winters 1998 and 2004 based on a cyclone tracking algorithm³⁴. We compute cyclone occurrence anomalies by counting the days per winter in which the respective grid cell is within the outermost closed isobar of the cyclones detected by the algorithm.

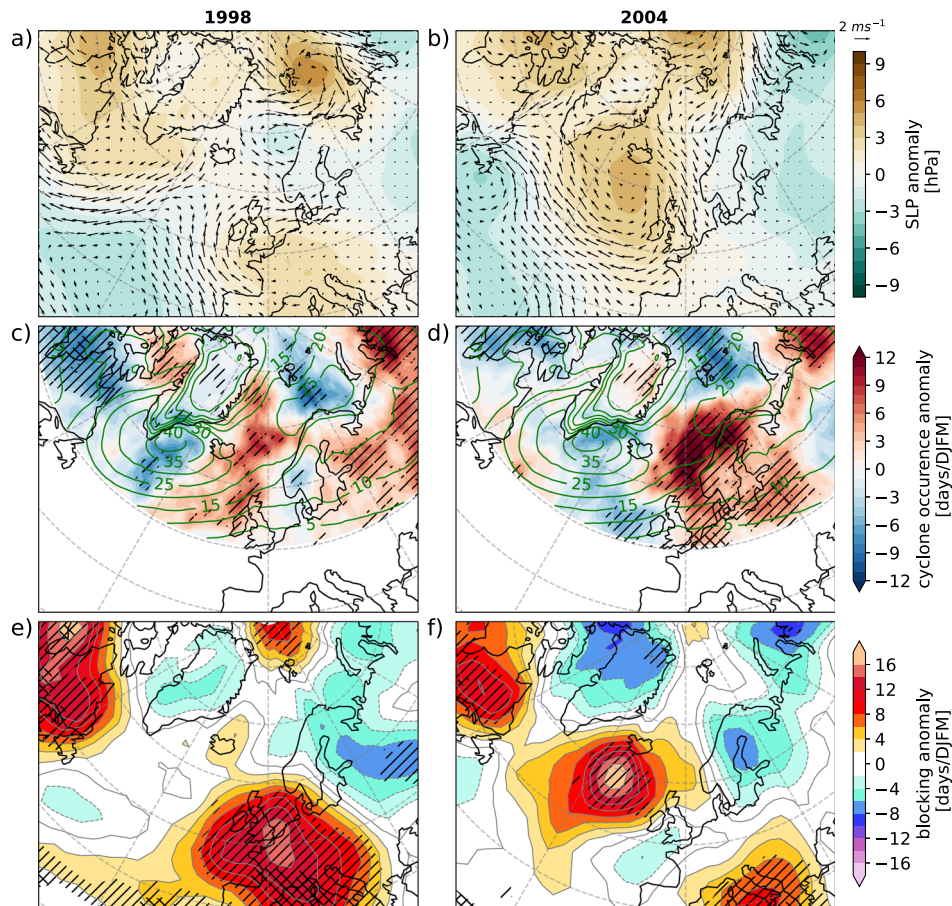


Fig. 5 Anomalous atmospheric circulation and cyclone occurrence in 1998 and 2004. Sea level pressure and wind anomalies of the winters (DJFM) 1998 and 2004 relative to the 1970–2019 winter mean from JRA55-do (a, b). Mean (1970–2019, green contours) and anomalous cyclone occurrence (color shading) of the respective winters (c, d). Note: Our cyclone database does not cover the region south of 50°N. Anomalous atmospheric blocking (e, f). Anomalies that exceeded one standard deviation are highlighted with black stripes, crisscrossed areas depict areas, where the anomaly exceeds two standard deviations of the respective quantity (c–f).

For the respective winters, cyclones show a tendency to move rather zonally towards the northern Norwegian coast instead of traveling along the regular winter storm track through the Norwegian Sea into the BS (Fig. 5c, d). In 2004, 12 additional days per winter under strong cyclonic activity (+60% compared to long-term mean) are counted near the Norwegian coast (Fig. 5d). The more zonal trajectories of the cyclones lead to less persistent alongshore wind anomalies at the Norwegian coast that would adjust the inflow. In addition, fewer days under cyclone influence (−9 days per winter in both 1998 and 2004, ca. −40%) are detected in the northern BS (Fig. 5c, d). This most likely contributes to the observed anticyclonic wind anomalies in the region in these winters. As a result of the cyclone deficit, the more anticyclonic flow over the northern BS shelf causes an acceleration of the outflow south of Bear Island, dominating the net transport anomalies in these years. The unusually zonal trajectories of synoptic cyclones in these particular years can be related to anomalous atmospheric blocking in the vicinity of Iceland and Great Britain (Fig. 5e, f). In 2004 (1998), +16 (+14) days per winter of anomalous atmospheric blocking seemingly forced cyclones on a more zonally route towards the Norwegian coast, thus resulting in a cyclone deficit in the BS.

In 2000 (2005), the NAO is in a pronounced positive (neutral) phase, but the upstream forced inflow anomalies (0.0 Sv in 2000, 0.28 Sv in 2005) do not follow the NAO forcing (Fig. 3c). In 2000, an increased pressure dipole between the Azores High (+9 hPa) and the Icelandic Low (−11 hPa) is present, which is in

accordance with the positive NAO phase. However, compared to the NAO pattern, the low pressure is located to the east of the Icelandic Low location and resides over the White Sea. Based on our analysis, we find the displacement of the low-pressure anomaly to be aligned with reduced blocking over Scandinavia, increased blocking over the northern North Atlantic, and anomalously high occurrence of cyclones in this winter (Fig. 6c, e). In the center of the low-pressure anomaly, a doubling of days under cyclone impact is detected (+20 days/winter) in both 2000 and 2005. Consequently, the surface wind anomalies resulting from the low-pressure anomaly in 2000 are directed perpendicular to the coastline (Fig. 6a) instead of being parallel to the coastline as in a normal case of positive NAO conditions. Despite the positive NAO in this winter, the anomalous surface winds do not affect the geostrophic flow of the NASC and thus do not significantly increase the BSO inflow. In 2005, a neutral NAO winter, no NAO-like pattern is found in the SLP anomaly (Fig. 6b). Instead, massively increased blocking (exceeding 2 standard deviations) in the North Atlantic sector forms a persistent anticyclonic circulation anomaly that, as in 2000, strongly deflects synoptic cyclones. The increased cyclone occurrence in the Nordic Seas in this winter results in the cyclonic alongshore wind anomaly, which further increases the BSO inflow despite the neutral NAO (Figs. 3c and 6b, d, f).

The winters 1994 (positive NAO, slightly negative upstream forced inflow anomaly) and 2001 (negative NAO, slightly positive upstream forced transport anomaly) further illustrate a

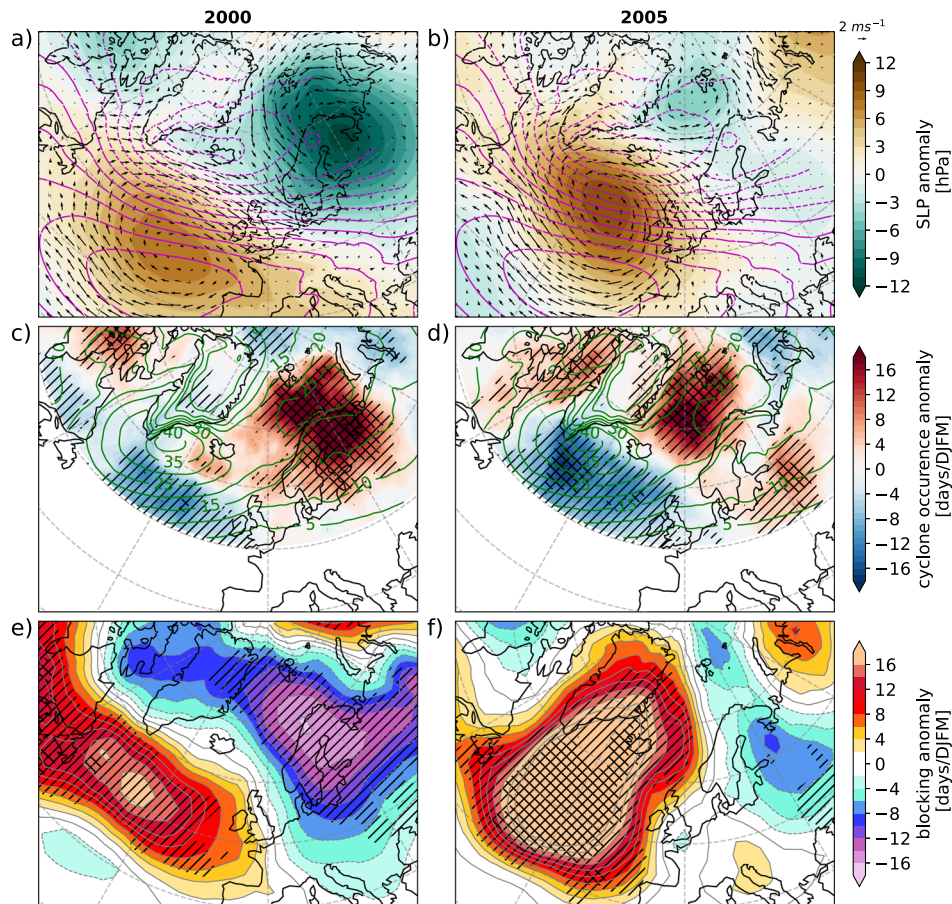


Fig. 6 Anomalous atmospheric circulation and cyclone occurrence in 2000 and 2005. All panels (a–f) as in Fig. 5a–f, but for the winters 2000 and 2005. In addition, the magenta lines in (a, b) depict the NAO pattern-related SLP anomaly as obtained from the EOF analysis. Note the modified color range in (a–d).

decoupling of the upstream forced BSO inflow from the NAO. Though the anomalous SLP in these winters matches the respective NAO state, winds at the Norwegian Atlantic coast do not represent the classical NAO pattern. In 2001, a strongly negative NAO would cause a strong northeast wind component at the Norwegian Atlantic coast, which would reduce the BSO inflow (Supplementary Fig. 1). However, the modification of the anomalously low cyclone occurrence on the SLP causes the along-coast component of the wind anomaly to be weak in this year (Fig. 7b, d). In 1994, the wind anomalies at the Norwegian coast are directed perpendicular to the coast, despite the positive NAO state which would suggest a more southwesterly wind anomaly in this area. The anomalously high cyclone occurrence modifies the low SLP pattern so that the anomalous wind is not directed along the coast (Fig. 7a, c). Extraordinary blocking anomalies (partly exceeding 2 standard deviations) are found in the North Atlantic sector in 1994 (−16 days/winter) and 2001 (−12 days/winter). In 1994, the low blocking increases the cyclone occurrence in the Norwegian Sea. In 2001, pronounced blocking occurred west of Greenland so the cyclone occurrence is reduced in the area around Greenland, including the Nordic Seas.

In summary, all 6 years support our hypothesis that anomalous regional atmosphere circulation patterns can heavily impact ocean transport through the BSO. Especially the loss of the NAO control on the BSO transport in the 1995–2005 period can specifically be attributed to anomalous atmospheric blocking which reshapes the North Atlantic storm track and the related synoptic cyclone activity in the Nordic Seas/BS domain affecting the ocean transport.

Discussion and conclusions

In this study, we disentangled locally and upstream forced contributions to ocean volume transport variability in the BSO and investigated their individual dependence on the NAO, the leading mode of climate variability in the North Atlantic sector. We found that the NAO cannot always explain the BSO transport variability, mainly due to changes in the spatial distribution of cyclones/NAO center of action associated with storm tracks in the Nordic Seas and the BS.

Wind variability associated with the NAO has been known to be a key factor controlling the ocean volume transport through the BSO^{18,21,27}. However, the high correlation between the NAO and the BSO inflow broke down around the year 2000¹⁸. We discovered that the loss of NAO control on the BSO inflow is only temporary. Our analysis further illustrates that the loss of NAO control in the 1995–2005 period can be related to six winters exhibiting anomalous propagation of cyclones causing (i) a temporary dominance of the outflow anomalies over the inflow anomalies in 1998 and 2004 due to significantly fewer cyclones reaching the northern BS and (ii) a shift of cyclone trajectories during pronounced NAO conditions in 1994, 2000, 2001, and 2005 resulting in strong deviations from the normal NAO related wind anomalies at the Norwegian Atlantic coast. Our results confirm a previous study on cyclone statistics in the vicinity of the BS, that found a temporary deficit in the number of cyclones on a northerly path affecting the BS in the 1995–2005 period³².

The exact fate of the NAO in a warmer future climate is yet unclear^{35–38}. By the end of the twenty-first century, it is

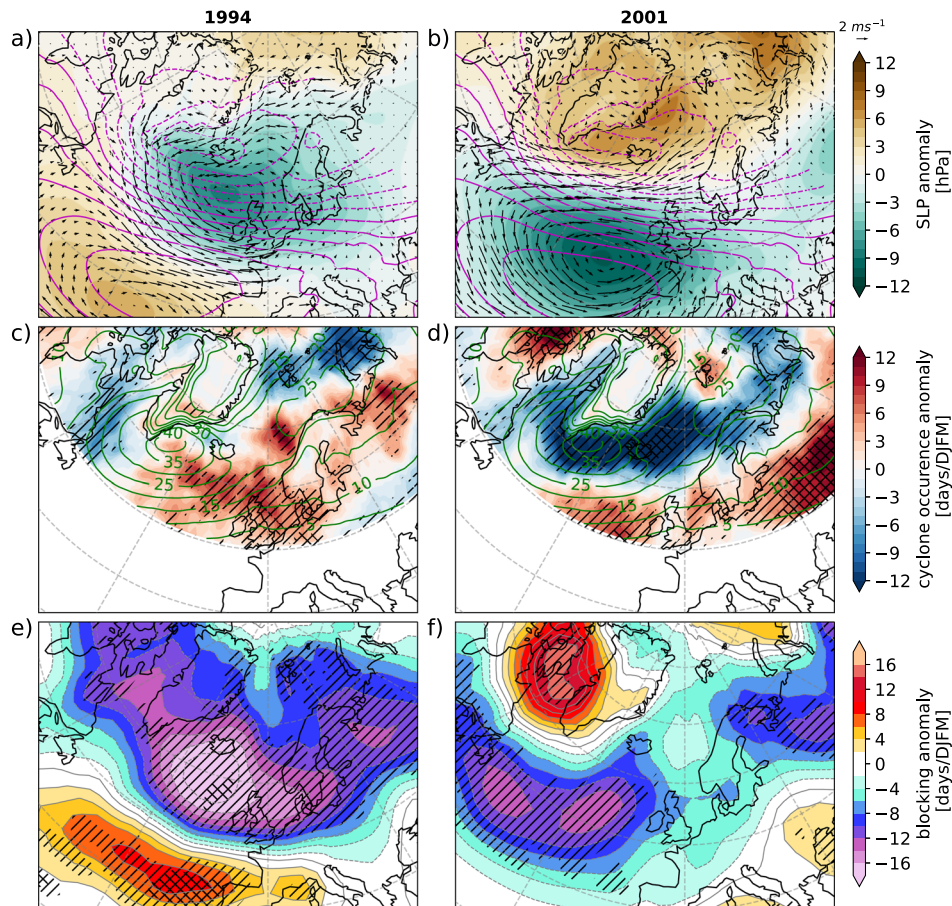


Fig. 7 Anomalous atmospheric circulation and cyclone occurrence in 1994 and 2001. All panels (a–f) as in Fig. 6a–f, but for the winters 1994 and 2001. Note the modified color range in (c, d).

projected that the characteristics of the NAO may be altered by anthropogenic forcing. Specifically, there may be a slight positive shift in the probability distribution of the NAO phase and a small northeastward displacement of its centers of action^{39–42}. As presented in this study, both, the NAO trend and displacement of the centers of action are relevant for the transports in the BSO. Oppositely, no NAO trend³⁸ or even a trend toward more negative NAO by an equatorward jet shift caused by Arctic warming³⁷ is also projected. Especially in wintertime, there is in general a lack of model agreement on the future NAO trend. In addition, El Niño and La Niña events can impact the state of the NAO, thus influencing the BSO transport⁴³.

The NAO state can also influence cyclone paths. A positive NAO leads to a northward shift in the storm tracks possibly resulting in fewer cyclones passing through BSO^{33,44}. Hence, along-coast winds in the BSO are less likely. In negative NAO conditions, storm tracks are at more southern locations. This observed co-variability of locally forced transport anomalies and the NAO during pronounced negative NAO conditions could become less relevant in a warmer future climate. For example, a more positive wintertime NAO as a result of increased CO₂ concentrations and a generally warmer climate would cause a more northerly storm track⁴⁵ and according to our findings a reduced impact of local forcing on the BSO transport anomalies. As the correlation between remotely forced transport anomalies in the BSO and the NAO is independent of the NAO state, anomalies forced remotely might become more dominant in the future. In addition, a shift of the NAOs' centers of action could impact cyclone propagation in

the North Atlantic sector and thus lead to a future change in the NAOs' control on BSO transports. However, no significant trends in the trajectories of synoptic cyclones reaching the vicinity of the Nordic Seas/BS in the 1979–2018 period were found³². In general, there is uncertainty regarding estimates of trends in cyclone occurrence and intensity in the Arctic over the past 40 years. Although some studies indicate an increase in cyclone depth and the occurrence of deep cyclones during winter³³, others report no significant changes⁴⁶ or a dependency on the period⁴⁷. Future projections in global and regional climate models have shown an increase of cyclone frequency in the Arctic in winter (DJF) and a decrease in summer (JJA) to the end of the twenty-first century under the Representative Concentration Pathway 8.5 scenario. About half of these projections further predicts winter cyclones to become weaker and smaller⁴⁶, which could affect transports in the BSO based on the results of this study.

The current absence of a trend in cyclone occurrence and the observed recovery of the NAO/BSO transport correlation after 2005 suggests internal variability as the main cause for the deflection of the cyclones and not the ongoing global warming. The importance of the NAO, cyclone activity, and their interaction with the BSO ocean volume transport indicates that climate models must adequately resolve the related atmospheric processes to better predict future Arctic climate change.

In addition, the ocean volume and heat transports into the BS are one of the major drivers of sea ice variability in the Barents and Kara Seas^{48,49}. An improved understanding of the volume and heat transports into the BS thus also leads to further advances

in our understanding of the sea ice variability as another large component of the Arctic climate system.

Methods

Model setup, experiment design, and evaluation. In this study, we use the Finite volume Sea Ice and Ocean Model (FESOM2.1)³¹. FESOM2.1 is formulated on a triangular mesh, allowing for regional refinement in a global ocean setup. FESOM2.1 and its precursor FESOM have been extensively applied for simulating the Arctic Ocean^{19,22,50–53}. In our experiments, we use a mesh with about 4.5 km grid size in the whole Arctic Ocean domain, including the Nordic Seas, and about 25 km in the adjacent seas. South of approximately 40°N, the horizontal resolution is set to nominal one degree (Supplementary Fig. S3a). Vertically the model is split into 46 z-layers with a thickness of 10 m close to the surface, increasing to 250 m in the deep ocean. All experiments are started from rest and initialized using the PHC3 hydrography⁵⁴.

In our model experiments, one part of the ocean domain is forced by atmospheric reanalysis forcing containing interannual variability, while the other is forced by a normal year atmospheric forcing without interannual variability. The choice of the two domains separates the Arctic from the rest of the globe. The boundaries separating the two domains are Fram Strait (76.5°N), BSO (17.5°E), Davis Strait (69°N), and Bering Strait (62°N) (Supplementary Fig. S3a). In the following, we refer to our three model simulations as CTRL, ArcVari, and ArcClim. In CTRL, the entire global model domain is forced with the Japanese 55-year Reanalysis of the atmosphere for driving ocean-sea-ice models⁵⁵ (JRA55-do) yielding a global hindcast simulation from 1958 until 2019. In ArcVari, atmospheric forcing outside the Arctic domain is replaced by NCEP-CORE1⁵⁶ (CORE1) normal year forcing that is repeated every year in the simulation. The normal year forcing is composed of a one-year annual cycle of 6-hourly atmospheric forcing fields, which represent the climatology of the atmosphere. In ArcClim, the CORE1 forcing is used in the Arctic domain and JRA55 elsewhere. These experiments allow us to separate the impact of inter-annually varying atmospheric processes inside and outside the Arctic domain on the BSO transport.

After a full 62-year cycle is performed as a spin-up for each experiment, the model runs are restarted from their respective final 2019 conditions for a second full cycle. The last 50 years of the second cycle (1970–2019) are evaluated in this study. The model yields monthly mean fields as output. In all experiments, hydrographic properties, sea ice area, as well as major currents in the BSO are well represented in the model (Supplementary Figs. S3 and S4). The model yields an annual mean BSO volume transport of 2.6 Sv, which is within the observational interannual range of 0.8 Sv to 2.9 Sv¹³ and further matches the synthesized estimate of 2.3 Sv¹⁸. Further, the BSO net transport shares the same seasonal variability as in the observations with increased transport during winter and minimum transport in early summer⁴⁸. All results in this study are based on winter (1st of December to 31st of March) means.

By combining forcing datasets, we create discontinuities along the border of the defined areas, which in the case of BSO section is close to BSO. The net transport anomalies as well as inflow anomalies and outflow anomalies in ArcVari and ArcClim almost perfectly add up to those of CTRL (Fig. 3a, c, e) proving the consistency of the transports when combining the forcing datasets even if the region of interest (BSO) is close to the forcing boundary. The small deviations of the transport anomalies between the sum of ArcClim and ArcVari and those of CTRL might be the result of discontinuities in the combined

forcing. As these are very small compared to the general magnitude of the transport variability, we consider the unwanted effect negligible. In addition, we investigated modifications of the velocity field of the BSO, such as the location of the main currents entering and leaving the BSO as well as the overall transport magnitude, in all simulations. The results are presented in Supplementary Fig. S4 and prove that neither the general velocity field across the BSO nor average net, inflow or outflow transports are strongly affected by the combining-forcing approach. In addition, mean temperature and salinity fields are not affected by the forcing approach, providing further evidence for the validity of the method.

Forcing interpolation. Using bilinear remapping, we spatially interpolated CORE1 to the JRA55 grid, applying the climate data operators (cdo remapbil). Temporally, nearest-neighbor interpolation was applied to interpolate the 6-hourly CORE1 forcing data to the 3-hourly JRA55 time axis.

Definition of winter means and anomalies. We define the winter mean as the average of the December–March period for each year in the 1970–2019 period. E.g., the winter 2000 relates to the average of 12/1999, 01/2000, 02/2000, and 03/2000. Anomalies are computed by removing the 1970–2019 mean and linearly detrending the data.

Definition of strong/weak transport events. Strong/weak BSO transport events used for composite analysis are defined as winters in which the detrended net transport anomalies are exceeding ± 1 standard deviation.

North Atlantic Oscillation definition. We compute the NAO pattern as the first empirical orthogonal function (EOF) of winter SLP (DJFM, 1958–2019) in the North Atlantic sector (20°–70°N; 90°W–40°E)²⁶ in the model forcing (JRA55-do). The associated timeseries of principal components (PC) is taken as the NAO index. NAO \pm events are defined as winters, in which the detrended winter NAO index exceeds ± 1 standard deviation.

Composite analysis. Composites are computed by averaging the linearly detrended atmospheric forcing data (DJFM means) during winters when a respective quantity exceeds ± 1 standard deviation.

Moving correlation. The correlation between the NAO and the transport anomalies is computed as the Pearson correlation coefficient in a moving window of 11 years in length to capture interannual to decadal co-variability. The results are largely independent of the window length (Supplementary Fig. S2). The associated year provides the center of the respective 11-year period (e.g., 2000 relates to the 1995–2005 period). Correlations are considered significant when they differ from 0 on a 95% confidence level based on a two-sided hypothesis test (Fisher transformation). Both the NAO and the respective transport component (11-year periods) are detrended before computing the correlation.

Regression/correlation analysis. We perform multivariate linear regression analysis:

$$V' = \alpha_j u_j + \beta_j v_j + c + \epsilon \quad (1)$$

where V' is the timeseries of detrended net transport anomalies, u_j and v_j are the detrended wind component anomalies at each

grid cell j , c is a constant, and ϵ the residual error term. We then reconstruct the transport anomalies at each grid point j based on the wind components u_j and v_j and the received regression coefficients α_j and β_j :

$$V_j^{rec} = \alpha_j u_j + \beta_j v_j \quad (2)$$

By correlating V' and V_j^{rec} at each grid cell, we finally receive maps highlighting regions where the wind variability can reasonably reproduce the variability of the transport through BSO and thus is likely to affect the BSO volume transport. Correlations are regarded as significant when they are different from 0 at a 95% confidence level (two-sided hypothesis test).

In addition, the regression coefficients α_j and β_j can be interpreted as a vector property

$$w_j = |\alpha_j, \beta_j|^{-1} \cdot (\alpha_j, \beta_j) \quad (3)$$

indicating the preferred wind direction of the regression fit.

Cyclone tracking algorithm. We make use of a cyclone detection and tracking algorithm³⁴ to analyze cyclone occurrence anomalies for specific winters. Cyclone occurrence is computed as days per winter that a specific grid cell is within the outermost closed isobar of a cyclone detected by the algorithm based on the sea level pressure of the JRA55-do reanalysis data⁵⁵ that is used to force the simulations. The anomaly is computed relative to the 1970–2019 winter (DJFM) mean. We only consider cyclones with a pressure difference of at least 10 hPa between the cyclone center and the outermost closed isobar.

2D atmospheric blocking. A two-dimensional (2D) atmospheric blocking index is used in this study⁵⁷. To compute the 2D blocking index, we have used the daily geopotential height at 500 mb extracted from the JRA55 reanalysis⁵⁸. The 2D blocking index is an extension of the one-dimensional (1D) Tibaldi-Molteni⁵⁹ (TM) to a two-dimensional map of blocking frequencies at every grid point. The southern geopotential height gradient (GHGS) and the northern geopotential height gradient (GHGN) for each grid point are evaluated as follows:

$$GHGS = \frac{Z(\Phi_0) - Z(\Phi_0 - 15^\circ)}{15^\circ} \quad (4)$$

$$GHGN = \frac{Z(\Phi_0 + 15^\circ) - Z(\Phi_0)}{15^\circ} \quad (5)$$

where ϕ_0 is the latitude of the considered grid point varying from 35°N to 75°N. For each month, we have calculated the ratio between the number of days when a certain grid point was blocked, i.e., the conditions $GHGS > 0$ and $GHGN < (-10 \text{ m per } ^\circ\text{lat})$ are simultaneously satisfied for at least 5 consecutive days.

Data availability

BSO temperature data are available at <https://ocean.ices.dk/core/iroc>. NCEP-CORE1 forcing data can be accessed at <https://data1.gfdl.noaa.gov/nomads/forms/mom4/CORE.html>, JRA55-do-v1.4 and JRA55 are stored at <https://climate.mri-jma.go.jp/pub/ocean/JRA55-do/> and <https://rda.ucar.edu/datasets/ds628-0/>, respectively. NSIDC sea ice concentration is available at <https://nsidc.org/data/g10010>. Data presented in this study are stored at <https://doi.org/10.5281/zenodo.8249639>.

Code availability

FESOM2.1 source code can be found at <https://github.com/FESOM/fesom2>. Analysis of FESOM2.1 model data was done with pyfesom2 (<https://github.com/FESOM/pyfesom2>). The specific model settings for the simulations, as well as the versions of the Python modules (anaconda environment) used for analyzing and visualizing the data, are stored at <https://doi.org/10.5281/zenodo.8249639>.

Received: 19 April 2023; Accepted: 31 August 2023;

Published online: 21 September 2023

References

- Skagseth, Ø. et al. Reduced efficiency of the Barents Sea cooling machine. *Nat. Clim. Change* **10**, 661–666 (2020).
- Shu, Q., Wang, Q., Song, Z. & Qiao, F. The poleward enhanced Arctic Ocean cooling machine in a warming climate. *Nat. Commun.* **12**, 1–9 (2021).
- Fosheim, M. et al. Recent warming leads to a rapid borealization of fish communities in the Arctic. *Nat. Clim. Change* **5**, 673–677 (2015).
- Sandø, A. B. et al. Barents Sea plankton production and controlling factors in a fluctuating climate. *ICES J. Mar. Sci.* **78**, 1999–2016 (2021).
- Wu, B., Handorf, D., Detloff, K., Rinke, A. & Hu, A. Winter weather patterns over Northern Eurasia and Arctic Sea ice loss. *Mon. Weather Rev.* **141**, 3786–3800 (2013).
- Lo, Y. T. E., Mitchell, D. M., Watson, P. A. G. & Screen, J. A. Changes in winter temperature extremes from future Arctic Sea-Ice loss and ocean warming. *Geophys. Res. Lett.* **50**, e2022GL102542 (2023).
- Lawrence, D. M., Slater, A. G., Tomas, R. A., Holland, M. M. & Deser, C. Accelerated Arctic land warming and permafrost degradation during rapid sea ice loss. *Geophys. Res. Lett.* **35**, 11506 (2008).
- Melia, N., Haines, K. & Hawkins, E. Sea ice decline and 21st century trans-Arctic shipping routes. *Geophys. Res. Lett.* **43**, 9720–9728 (2016).
- Buckley, M. W. & Marshall, J. Observations, inferences, and mechanisms of the Atlantic meridional overturning circulation: a review. *Rev. Geophys.* **54**, 5–63 (2016).
- Furevik, T. Annual and interannual variability of Atlantic Water temperatures in the Norwegian and Barents Seas: 1980–1996. *Deep Sea Res. Part I Oceanographic Res. Papers* **48**, 383–404 (2001).
- Ingvaldsen, R., Loeng, H. & Asplin, L. Variability in the Atlantic inflow to the Barents Sea based on a one-year time series from moored current meters. *Cont. Shelf Res.* **22**, 505–519 (2002).
- Orvik, K. A. & Skagseth, Ø. Heat flux variations in the eastern Norwegian Atlantic Current toward the Arctic from moored instruments, 1995–2005. *Geophys. Res. Lett.* **32**, 1–5 (2005).
- Skagseth, Ø. et al. Volume and heat transports to the Arctic Ocean via the Norwegian and Barents seas. *Arctic-Subarctic Ocean Fluxes: Defining the Role of the Northern Seas in Climate* 45–64. https://doi.org/10.1007/978-1-4020-6774-7_3/COVER (2008).
- Skagseth, Ø., Orvik, K. A. & Furevik, T. Coherent variability of the Norwegian Atlantic Slope Current derived from TOPEX/ERS altimeter data. *Geophys. Res. Lett.* **31**. <https://doi.org/10.1029/2004GL020057> (2004).
- Orvik, K. A. & Skagseth, Ø. The impact of the wind stress curl in the North Atlantic on the Atlantic inflow to the Norwegian Sea toward the Arctic. *Geophys. Res. Lett.* **30**. <https://doi.org/10.1029/2003GL017932> (2003).
- Lien, V. S., Vikebø, F. B. & Skagseth, Ø. One mechanism contributing to co-variability of the Atlantic inflow branches to the Arctic. *Nat. Commun.* **4**, 1–6 (2013).
- Smedsrud, L. H., Ingvaldsen, R., Nilsen, J. E. Ø. & Skagseth, Ø. Heat in the Barents Sea: transport, storage, and surface fluxes. *Ocean Sci.* **6**, 219–234 (2010).
- Smedsrud, L. H. et al. The role of the Barents Sea in the Arctic climate system. *Rev. Geophys.* **51**, 415–449 (2013).
- Heukamp, F. O., Kanzow, T., Wang, Q., Wekerle, C. & Gerdes, R. Impact of cyclonic wind anomalies caused by massive winter sea ice retreat in the Barents Sea on Atlantic water transport toward the Arctic: a model study. *J. Geophys. Res. Oceans* **128**, e2022JC019045 (2023).
- Ingvaldsen, R. B., Asplin, L. & Loeng, H. The seasonal cycle in the Atlantic transport to the Barents Sea during the years 1997–2001. *Cont. Shelf Res.* **24**, 1015–1032 (2004).
- Ingvaldsen, R. B., Asplin, L. & Loeng, H. Velocity field of the western entrance to the Barents Sea. *J. Geophys. Res. Oceans* **109**. <https://doi.org/10.1029/2003JC001811> (2004).
- Wang, Q. et al. Ocean heat transport into the Barents Sea: distinct controls on the upward trend and interannual variability. *Geophys. Res. Lett.* **46**, 13180–13190 (2019).
- Blindheim, J. et al. Upper layer cooling and freshening in the Norwegian Sea in relation to atmospheric forcing. *Deep Sea Res. Part I Oceanographic Res. Papers* **47**, 655–680 (2000).
- Hurrell, J. W., Kushnir, Y. & Visbeck, M. The North Atlantic oscillation. *Science* **291**, 603–605 (2001).
- Hurrell, J. W. & Deser, C. North Atlantic climate variability: the role of the North Atlantic Oscillation. *J. Mar. Syst.* **79**, 231–244 (2010).
- Hurrell, J. W. et al. Decadal trends in the North Atlantic Oscillation: regional temperatures and precipitation. *Science* **269**, 676–679 (1995).

27. Ingvaldsen, R., Loeng, H., Ottersen, G. & Ådlandsvik Ingvaldsen, B. Climate variability in the Barents Sea during the 20th century with a focus on the 1990s. *ICES Mar. Sci. Symp.* **219**, 160–168 (2003).
28. Dickson, R. R. et al. The Arctic Ocean response to the North Atlantic Oscillation. *J. Clim.* **13**, 2671–2696 (2000).
29. Serreze, M. C., Carse, F., Barry, R. G. & Rogers, J. C. Icelandic low cyclone activity: climatological features, linkages with the NAO, and relationships with recent changes in the northern hemisphere circulation. *J. Clim.* **10**, 453–464 (1997).
30. Deser, C., Walsh, J. E. & Timlin, M. S. Arctic sea ice variability in the context of recent atmospheric circulation trends. *J. Clim.* **13**, 617–633 (2000).
31. Danilov, S., Sidorenko, D., Wang, Q. & Jung, T. The finite-volume sea ice–ocean model (FESOM2). *Geosci. Model Dev.* **10**, 765–789 (2017).
32. Madonna, E., Hes, G., Li, C., Michel, C. & Siew, P. Y. F. Control of Barents Sea wintertime cyclone variability by large-scale atmospheric flow. *Geophys. Res. Lett.* **47**. <https://doi.org/10.1029/2020GL090322> (2020).
33. Zahn, M., Akperov, M., Rinke, A., Feser, F. & Mokhov, I. I. Trends of cyclone characteristics in the Arctic and their patterns from different reanalysis data. *J. Geophys. Res. Atmos.* **123**, 2737–2751 (2018).
34. Akperov, M., Semenov, V. A., Mokhov, I. I., Dorn, W. & Rinke, A. Impact of Atlantic water inflow on winter cyclone activity in the Barents Sea: insights from coupled regional climate model simulations. *Environ. Res. Lett.* **15**, 024009 (2020).
35. Deser, C., Hurrell, J. W. & Phillips, A. S. The role of the North Atlantic Oscillation in European climate projections. *Clim. Dyn.* **49**, 3141–3157 (2017).
36. Deser, C., Magnusdottir, G., Saravanan, R. & Phillips, A. The effects of North Atlantic SST and sea ice anomalies on the winter circulation in CCM3. Part II: direct and indirect components of the response. *J. Clim.* **17**, 877–889 (2004).
37. Screen, J. A., Simmonds, I., Deser, C. & Tomas, R. The atmospheric response to three decades of observed Arctic sea ice loss. *J. Clim.* **26**, 1230–1248 (2013).
38. Cusinato, E., Rubino, A. & Zanchettin, D. Winter Euro-Atlantic climate modes: future scenarios from a CMIP6 multi-model ensemble. *Geophys. Res. Lett.* **48**. <https://doi.org/10.1029/2021GL094532> (2021).
39. Ulbrich, U. & Christoph, M. A shift of the NAO and increasing storm track activity over Europe due to anthropogenic greenhouse gas forcing. *Clim. Dyn.* **15**, 551–559 (1999).
40. Branstator, G. & Selten, F. “Modes of variability” and climate change. *J. Clim.* **22**, 2639–2658 (2009).
41. Deser, C., Phillips, A., Bourdette, V. & Teng, H. Uncertainty in climate change projections: the role of internal variability. *Clim. Dyn.* **38**, 527–546 (2012).
42. Barnes, E. A. & Polvani, L. M. CMIP5 projections of Arctic amplification, of the North American/North Atlantic circulation, and of their relationship. *J. Clim.* **28**, 5254–5271 (2015).
43. Luo, B. et al. Origins of Barents-Kara sea-ice interannual variability modulated by the Atlantic pathway of El Niño–Southern Oscillation. *Nat. Commun.* **14**, 1–13 (2023).
44. Vessey, A. F., Hodges, K. I., Shaffrey, L. C. & Day, J. J. An inter-comparison of Arctic synoptic scale storms between four global reanalysis datasets. *Clim. Dyn.* **54**, 2777–2795 (2020).
45. Stephenson, D. B., Pavan, V., Collins, M., Junge, M. M. & Quadrelli, R. North Atlantic Oscillation response to transient greenhouse gas forcing and the impact on European winter climate: a CMIP2 multi-model assessment. *Clim. Dyn.* **27**, 401–420 (2006).
46. Akperov, M. et al. Future projections of cyclone activity in the Arctic for the 21st century from regional climate models (Arctic-CORDEX). *Glob. Planet Change* **182**, 103005 (2019).
47. Valkonen, E., Cassano, J. & Cassano, E. Arctic cyclones and their interactions with the declining sea ice: a recent climatology. *J. Geophys. Res. Atmos.* **126**, e2020JD034366 (2021).
48. Årthun, M., Eldevik, T., Smedsrud, L. H., Skagseth, Ø. & Ingvaldsen, R. B. Quantifying the influence of Atlantic heat on Barents sea ice variability and retreat. *J. Clim.* **25**, 4736–4743 (2012).
49. Lien, V. S., Schlichtholz, P., Skagseth, Ø. & Vikebø, F. B. Wind-driven Atlantic water flow as a direct mode for reduced Barents Sea ice cover. *J. Clim.* **30**, 803–812 (2017).
50. Wang, Q. et al. Intensification of the Atlantic water supply to the Arctic Ocean through Fram Strait induced by Arctic Sea ice decline. *Geophys. Res. Lett.* **47**. <https://doi.org/10.1029/2019GL086682> (2020).
51. Wekerle, C., Wang, Q., Danilov, S., Jung, T. & Schröter, J. The Canadian Arctic Archipelago throughflow in a multiresolution global model: model assessment and the driving mechanism of interannual variability. *J. Geophys. Res. Oceans* **118**, 4525–4541 (2013).
52. Wekerle, C. et al. Eddy-resolving simulation of the Atlantic Water circulation in the Fram Strait with focus on the seasonal cycle. *J. Geophys. Res. Oceans* **122**, 8385–8405 (2017).
53. Wang, Q. et al. Eddy kinetic energy in the Arctic Ocean from a global simulation with a 1-km Arctic. *Geophys. Res. Lett.* **47**. <https://doi.org/10.1029/2020GL088550> (2020).
54. Steele, M., Morley, R. & Ermold, W. PHC: a global ocean hydrography with a high-quality Arctic ocean. *J. Clim.* **14**, 2079–2087 (2001).
55. Tsujino, H. et al. JRA-55 based surface dataset for driving ocean–sea-ice models (JRA55-do). *Ocean Model* **130**, 79–139 (2018).
56. Yeager, S. G. Diurnal to decadal global forcing for ocean and sea-ice models: the data sets and flux climatologies coordinated ocean-ice reference experiments view project. <https://doi.org/10.5065/D6KK98Q6> (2004).
57. Scherrer, S. C., Croci-Maspoli, M., Schwierz, C. & Appenzeller, C. Two-dimensional indices of atmospheric blocking and their statistical relationship with winter climate patterns in the Euro-Atlantic region. *Int. J. Climatol.* **26**, 233–249 (2006).
58. KOBAYASHI, S. et al. The JRA-55 reanalysis: general specifications and basic characteristics. *J. Meteorol. Soc. Jpn. Ser. II* **93**, 5–48 (2015).
59. TIBALDI, S. & MOLTENI, F. On the operational predictability of blocking. *Tellus A* **42**, 343–365 (1990).

Acknowledgements

We gratefully acknowledge the funding by the Deutsche Forschungsgemeinschaft (DFG, German Research Foundation) through the Transregional Collaborative Research Centre TRR-172 “Arctic Amplification: Climate Relevant Atmospheric and Surface Processes, and Feedback Mechanisms (AC)^{3m}” (grant 268020496). A.R. acknowledges funding by the European Union’s Horizon 2020 research and innovation framework program under Grant agreement no.101003590 (PolarRES project). M.I. was partially supported by BMBF through the project “Abrupt Climate Shifts and Extremes over Eurasia in Response to Arctic Sea Ice Change (ACE)³” under Grant 01LP2004A. We would like to thank Mirseid Akperov for providing the cyclone detection and tracking data. Furthermore, this work was supported by the North-German Supercomputing Alliance (HLRN). We are grateful to the HLRN super-computer staff, for providing the infrastructure allowing us to perform this research.

Author contributions

F.O.H. designed the study, carried out the model experiments, and wrote the paper draft. L.A. analyzed the cyclone data. Q.W. and C.W. assisted in setting up and executing the model simulations. M.I. carried out the atmospheric blocking analysis. T.K. and A.R., as well as all other coauthors, assisted in interpreting and contextualizing the results. All coauthors were involved in reviewing and finalizing the manuscript.

Funding

Open Access funding enabled and organized by Projekt DEAL.

Competing interests

The authors declare no competing interests.

Additional information

Supplementary information The online version contains supplementary material available at <https://doi.org/10.1038/s43247-023-00985-1>.

Correspondence and requests for materials should be addressed to Finn Ole Heukamp.

Peer review information *Communications Earth & Environment* thanks Vidar Lien and the other, anonymous, reviewer(s) for their contribution to the peer review of this work. Primary Handling Editors: Jennifer Veitch, Heike Langenberg. A peer review file is available.

Reprints and permission information is available at <http://www.nature.com/reprints>

Publisher’s note Springer Nature remains neutral with regard to jurisdictional claims in published maps and institutional affiliations.



Open Access This article is licensed under a Creative Commons Attribution 4.0 International License, which permits use, sharing, adaptation, distribution and reproduction in any medium or format, as long as you give appropriate credit to the original author(s) and the source, provide a link to the Creative Commons license, and indicate if changes were made. The images or other third party material in this article are included in the article’s Creative Commons license, unless indicated otherwise in a credit line to the material. If material is not included in the article’s Creative Commons license and your intended use is not permitted by statutory regulation or exceeds the permitted use, you will need to obtain permission directly from the copyright holder. To view a copy of this license, visit <http://creativecommons.org/licenses/by/4.0/>.

© The Author(s) 2023